MICROSTRUCTURE AND CRYSTALLOGRAPHIC TEXTURE OF A NEAR-BETA TITANIUM ALLOY FABRICATED BY LASER POWDER BED FUSION WITH A FLAT-TOP LASER BEAM

Tomonori Kitashima[1,2], Dennis Edgard Jodi[1,2], Makoto Watanabe[1]

1 National Institute for Materials Science, 1-2-1 Sengen, Tsukuba, Ibaraki, 305-0047 Japan.
2 Department of Materials, Kyushu University, 744 Motooka Nishi-ku, Fukuoka, 819-0395 Japan.

A near-β Ti-6Al-2Sn-4Zr-6Mo alloy (Ti-6246) was fabricated by laser powder bed fusion using a flat-top laser beam, and its microstructure and texture were investigated. Fabrication was carried out using an SLM 280 HL equipped with a flat-top laser beam, 700 μm in diameter. A single fusion track was initially analyzed using a Ti-6246 plate without powder. The melt-pool depth decreased with increasing laser scan speed under constant laser power, and the melt-pool geometry shifted from super-Gaussian to planar. However, a smaller melt-pool depth led to a less stable melt-pool geometry. By using optimized parameters to achieve a planar melt pool geometry via fusion track analysis, grain growth occurred parallel to the build direction in the powder bed fusion. This resulted in a near-{001}<100> β texture formation on the plane perpendicular to the build direction. This could be because the direction of local thermal gradients at the solid–liquid interface of the bottom of the melt pool was aligned parallel to the build direction. Very thin grain α phases and fine grain interior acicular α phases were formed. The melt-pool geometry and texture formation can be controlled by combining flat-top laser and Gaussian beams in laser powder bed fusion.

Keywords: Laser powder bed fusion, flat-top laser beam, titanium, texture, grain growth, melt pool.

1. Introduction

Additive manufacturing is an effective process for manufacturing jet engine parts. Controlling the grain structure and microstructure of engine parts during manufacturing is crucial for achieving high performance. There have been various reports on the effects of fabrication parameters and scan strategies on the grain structure and defect formation in laser powder bed fusion (LPBF) for Ti alloys [1–5]. Previous reports adopted a Gaussian laser beam that possesses a Gaussian profile intensity on the irradiated plane (Figure 1(a)). This results in a large temperature gradient from the center to the edge across the irradiated surface. Researchers have been able to control the crystallographic textures with a Gaussian laser beam by adopting different scan strategies. For example, Ishimoto *et al.* demonstrated that bidirectional scanning with and without a 90° rotation between layers led to different textures with preferential orientations of <001> and <011> along the building direction, respectively, in the Ti-15Mo-5Zr-3Al alloy [1]. Jodi *et al.* recently demonstrated the feasibility of producing a single-crystal structure of pure Ni using a flat-top laser beam profile with a uniform intensity on the irradiated surface (Figure 1(b)) [6]. The optimization of the fabrication parameters allowed the formation of a planar melt pool, which promoted the growth of <001>-oriented solidification grains almost parallel to the build direction (BD). Gradually, <001>-oriented grains become dominant over grains grown in other orientations, leading to the suppression of high-angle grain boundaries (HAGBs) formation. Finally, a single-crystal structure with homogeneous <001> texture was obtained. However, it contained low-angle grain boundaries (LAGBs) and sub grains. Thus, obtaining a planar melt pool using a flat-top laser beam is a useful approach for aligning the grain structure in a way that differs from conventional methods. However, there have been few reports on the texture formation of near-β Ti alloys with α precipitates fabricated using a flat-top laser beam [7]. In this study, a near-β Ti-6Al-2Sn-4Zr-6Mo alloy (Ti-6246) was fabricated by LPBF using a flat-top laser beam, and its microstructure and crystallographic texture were investigated and compared with those obtained using a Gaussian laser beam instead of a flat-top laser beam.

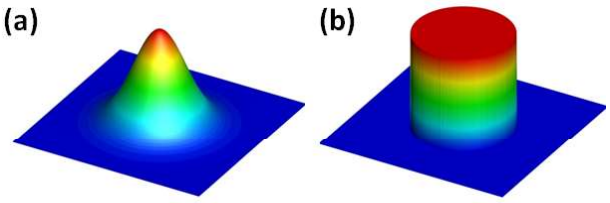

Figure 1. Schematics of the intensity distribution on the plane perpendicular to the laser irradiated direction for (a) Gaussian and (b) flat-top laser beams.

2. Experimental procedures

The fabrication was performed in an Ar atmosphere using an SLM 280 HL (SLM Solutions, Germany). The SLM apparatus comprised flat-top laser and Gaussian lasers with beam diameters (d_b) of 700 and 80 μm, respectively. Single tracks were analyzed to observe the melt pool geometry using Ti-6246 plates (TIMET, USA) without a powder layer coating. The power (P) and scan speed (v) of the laser in the single-track analysis varied between 250–350 W, 600–1500

mm/s, respectively, for the Gaussian beam. For the flat-top beam, the scan speed ranged from 100–550 mm/s. The melt-pool geometry was observed on the build direction (BD)–hatch direction (HD) plane, which is perpendicular to the scanning direction (SD). Multilayers were fabricated in the powder bed fusion using the *P*–*v* combination of the observed melt pool geometry. The energy density (E_M) was obtained for multiple multi-layers using the following equation [8]:

$$E_M = \frac{\beta P}{h\sqrt{4\alpha d_b v}}, \quad (1)$$

where, β and α represent absorption factor (~0.8) and thermal diffusivity (~2.55 mm^2/s), respectively. The parameters used for fabricating the multilayers and the energy densities calculated from these parameters are listed in Table 1. The layer thickness was maintained at 30 µm during fabrication. Plasma-atomized Ti-6246 powder (Advanced Powders & Coatings, Inc., Canada) was used. D_{10}, D_{50}, and D_{90} values of the powder were ~25.3, ~41.1, and ~63.7 µm, respectively. The laser was used to scan in a zigzag manner, with a 90° rotation for each layer, during the multilayer fabrication. Cylindrical specimens (12 mm in diameter and 30 mm in height) were fabricated on pure Ti plates, as shown in Figure 2. In this study, the powder stage was not heated. All specimens were sectioned and ground with abrasive paper (#320 and #600) and mechanically polished using diamond (9, 3, and 1 µm) and colloidal silica suspensions. Scanning electron microscopy (SEM; JEOL JSM-7001F) and electron backscatter diffraction (EBSD) were used to characterize the microstructure of the specimens. The EBSD analysis was conducted on the HD–BD cross-section with minimum measuring areas of 800×1200 µm and a step size of 4 µm. The EBSD data were analyzed using TSL OIM 8. In this study, LAGBs and HAGBs were classified based on misorientations, with LAGBs and HAGBs having misorientations ranging from 5°–15° and >15°, respectively. The constituent phases were identified by X-ray diffraction (XRD) analysis using a SmartLab diffractometer (Rigaku, Japan) with Cu Kα (λ = 1.5418 A) radiation generated at 45 kV and 200 mA.

3. Results and discussion

3.1. Single-fusion track analysis

Single-fusion tracks were initially analyzed to investigate the correlation between the fabrication parameters, particularly the laser scan speed and melt-pool geometry. Figure 3 shows the backscattered electron (BSE) images of the cross-section of the fusion tracks scanned by the Gaussian laser beam. As the laser scan speed increased, the melt pool became shallower and narrower because of the decreased energy density.

Table 1: Fabrication parameters in this study.

	Laser power (W)	Laser scan speed (mm/s)	Hatch space (µm)	Energy density (J/mm^3)
G1	300	1500	90	76.22
FT1	300	350	110	43.65
FT2	300	250	120	47.34

Figure 2. Fabricated cylindrical specimens. Diameter: 12 mm and height: 30 mm.

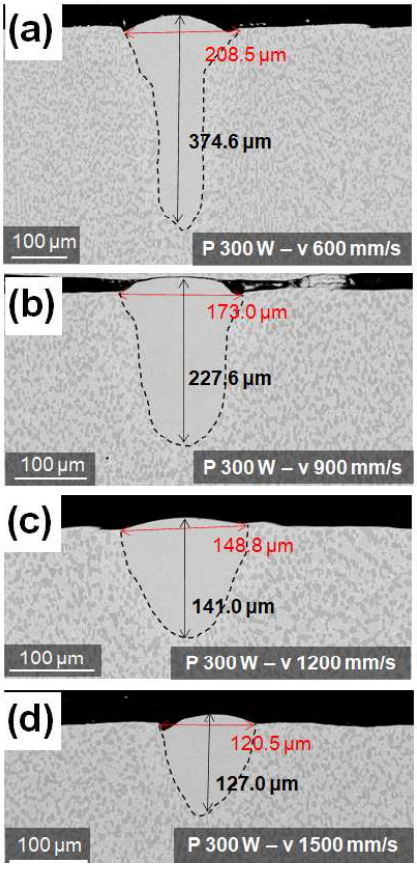

Figure 3. Cross sections of the plate fusion tracks scanned by Gaussian beam.

At 600 mm/s, the melt pool was deep, whereas at 1500 mm/s, the geometry was semi-elliptical. In contrast, when the flat-top laser beam was used to scan for a single track, the melt pool became shallower and narrower as the laser scan speed increased, as shown in Figure 4. This trend is similar to that observed with the Gaussian laser beam, although the melt pool geometry with the flat-top laser beam was significantly shallower than that obtained with the Gaussian laser beam. The geometry of the planar melt pool caused by the flat-top laser beam becomes unstable and asymmetric at scan speeds greater than 350 mm/s (Figure 4(c)–(e)). Different ranges of the laser scan speed were adopted for the Gaussian and flat-top laser beams as shown in Figures 3 and 4. Because these beam diameters are different, the energy densities are different for the same fabrication parameters. For example, when the laser scan speed was set to 1500 mm/s with a laser power of 300 W on a single track using a flat-top laser, the plate melted partially.

3.2. Multi-layer fabrication

Figure 5 shows the BSE images of the cross section parallel to the BD at the center, specifically at the height of 29.5 mm, for the multilayered specimens of G1 (a, c) and FT2 (b, d).

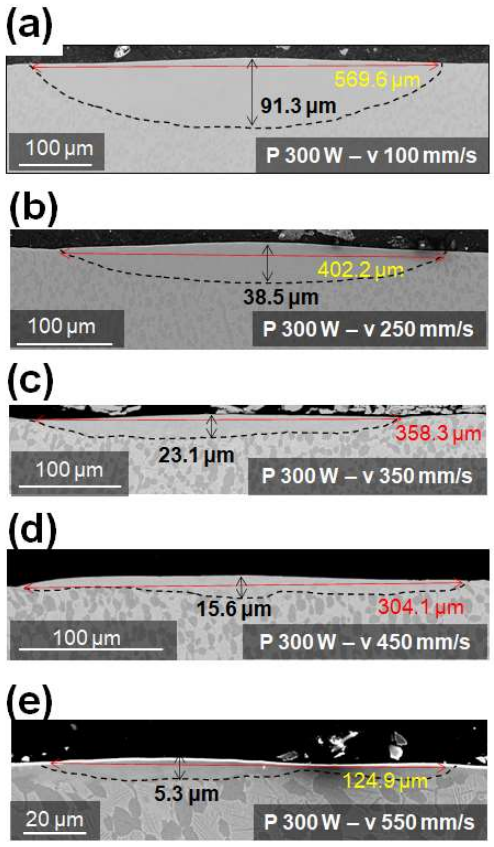

Figure 4. Cross sections of the plate fusion tracks scanned by flat-top beam.

The laser power and scan speed of G1 and FT2 were the same as those used in the semi-elliptical and planar melt pools, respectively, as shown in Figures 3(d) and 4(b). The grain boundaries are indicated by the dashed lines in Figures 5(a) and (b). Figures 5(c) and (d) show the magnified grain boundary (GB) α in Figures 5(a) and (b), respectively. For both G1 and FT2, columnar grains grew in the BD. However, the widths of the grown grains were relatively uniform in G1, but not in FT2. This is because during the solidification of the melt pool, due to the Gaussian laser beam, the grains grew toward the melt pool center and upward from the semi-elliptical fusion line in the direction perpendicular to the fusion line on the HD–BD plane. The HAGBs then formed at the center line as a "laser trail." However, in FT2, such "laser trails" were not observed because the <001>-oriented growth, parallel to the BD, caused negligible angle differences between grain growth directions on the fusion line on the HD–BD plane. This will be discussed later using the EBSD results. In the XRD analysis, the peaks of α–α" and α–β were detected for G1 and FT2, respectively. This is because the cooling rate during the fabrication of G1 was very high, and martensitic α" was transformed from the β phase soon after solidification. In contrast, the cooling rate of FT2 may be slower, and/or the layer-by-layer heat cycles during the shallow-melt-pool formation continued to heat the solidified layers during fabrication. This resulted in the transformations of β to α" and α–β after solidification [9]. For both G1 and FT2, the GB α was formed with a thickness of less than 100 nm, as shown in Figure 5. However, the thickness of GB α was thinner in G1, which has a lower cooling rate than FT2. In addition, very fine acicular phases precipitated in grains of both G1 and FT2 although the grain-interior α in FT2 was more distinguishable with larger sizes.

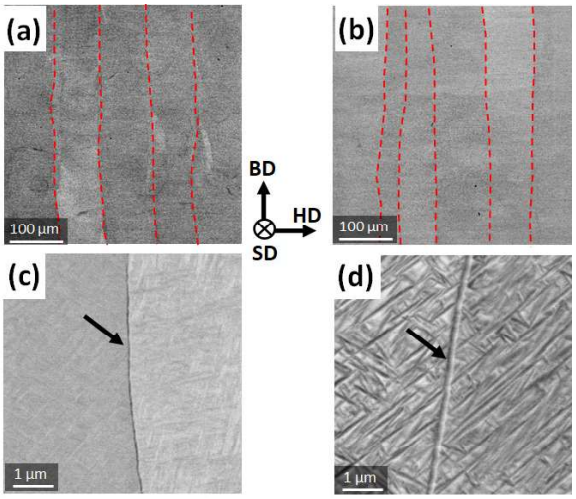

Figure 5. Cross sections perpendicular to the build direction for multi-layered specimens fabricated using (a, c) Gaussian and (b, d) flat top laser beams. (a) and (c): G1; (b) and (d): FT2.

Figures 6(a–c) and (d–f) show the inverse pole figure (IPF) maps for β phase and phase maps for α/β phases, respectively, on the cross-section parallel to the BD for G1, FT1 and FT2 at the center, specifically at the height of 29.5 mm. The β-phase IPF maps (Figures 6 (a–c)) were obtained as IPF-Z for the texture perpendicular to the BD. The atomic positions in the orthorhombic α" phase are close to those in the cubic β phase, leading to similarly indexed EBSD patterns. Therefore, the α" texture was characterized using the crystal parameters of β-Ti in the EBSD analysis [10]. In G1 and FT1, the <001>–<111> texture was observed as shown in Figures 6(a) and (b). However, the "laser trails" were clearly observed in G1. In FT2, A homogeneous <001>β-texture was obtained (Figure 6(c)), although the α phase was dominant in the as-fabricated microstructure, as shown in Figure 6(f). The α phase fractions were 0.47, 0.60, and 0.77 for G1, FT1, and FT2, respectively.

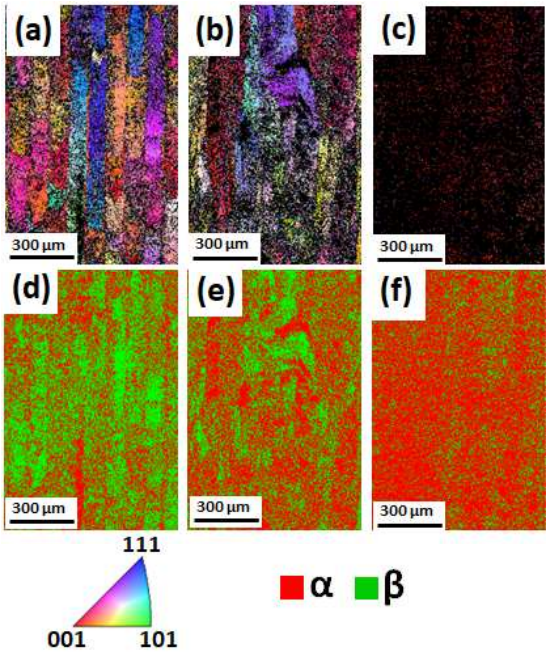

Figure 6. (a–c) β-phase IPF map and (d–f) α/β-phase map on the cross-section parallel to the BD. The β-phase IPF map shows the texture perpendicular to the BD (IPF-Z). (a) and (d): G1, (b), (e): FT1, (c) and (f): FT2.

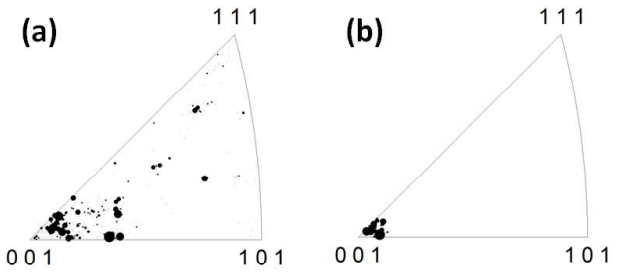

Figure 7. β-phase-grain orientations and sizes for (a) G1 and (b) FT2. These were obtained from the areas of Figure 6(a) and (c), respectively.

Figures 7(a) and (b) shows maps of each β-phase grain orientation and size for G1 and FT2, respectively. These were obtained from the areas shown in Figures 6(a) and (c), respectively. The G1 grains exhibited various orientations on the plane perpendicular to the BD, whereas FT2 exhibited <001>-oriented grains. One reason for this difference is that the texture formation depends on the melt pool geometry. In the melt pool caused by the Gaussian laser beam, the grains grew in the direction of the highest temperature gradient from the semi-elliptical fusion line, that is, perpendicular to the fusion line on the HD–BD plane, as mentioned previously.

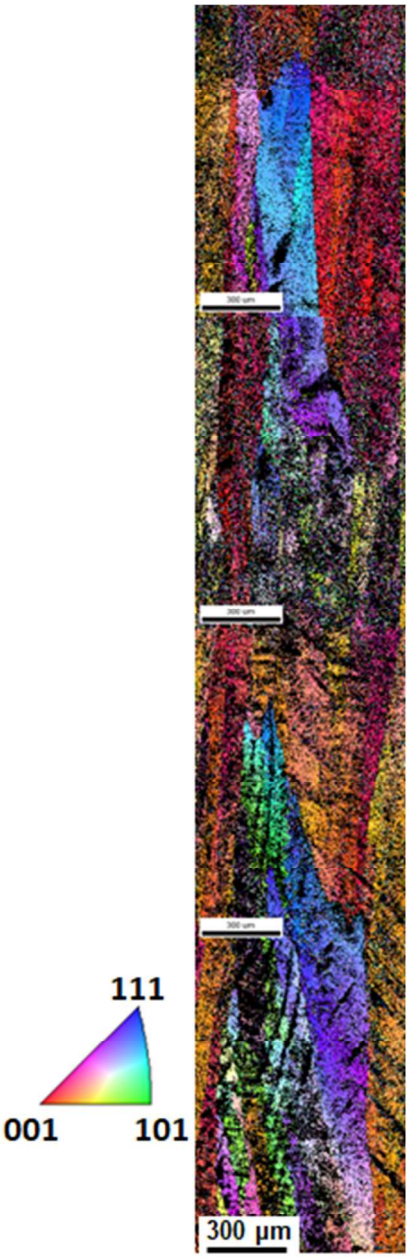

Figure 8. The β-phase IPF map of FT1 on the cross-section parallel to the build direction, which shows the texture perpendicular to the BD.

In contrast, for the flat-top-laser-derived melt pool, the grains grew in a direction close to the BD on the HD–BD plane because of the planar melt pool geometry. However, the β-texture for FT1 was composed of grains of various orientations, as shown in Figure 6(b), although the melt pool geometry was planar in Figure 4(c) in the fusion track analysis. As the energy density of the flat-top laser beam decreased, the melt pool became increasingly shallower and narrower. In addition, the geometry became unstable and asymmetric. This asymmetry may be unfavorable for controlling the grain growth in the direction aligned to the fusion line.

The LPBF process generates a high thermal gradient-to-cooling rate (G/R) ratio owing to the smaller melt pool size in comparison to the surrounding powder bed. In addition, the small distance between the melt-pool bottom and melt-pool surface prevents significant undercooling, particularly for melt pools with small depths. Moreover, equiaxed grains do not form from bulk homogeneous nucleation without a high density of solid particles or partially unmelted powder. Therefore, in LPBF, epitaxial growth predominantly occurs from the melt-pool fusion line, taking on the crystal structure and orientation of the lower layer. The <001>orientation of cubic crystals, such as body-centered cubic (bcc) and face-centered cubic (fcc) crystals, preferentially grows along the direction of the highest temperature gradient at the fusion line. Figure 8 shows the IPF map of FT1 for the HD–BD cross-section at the center top of the specimen. The texture on the plane perpendicular to the BD is shown here. The EBSD analysis area in Figure 8 is 800×4800 μm with a step size of 4 μm. In FT1, grains grew upward epitaxially even though each layer thickness was 30 μm. The <001>–<111> textures appear asymmetrically and periodically. To obtain a homogeneous <001>-texture on the HD–scanning direction (SD) plane, it is important to optimize the fabrication parameters and render the planar and symmetrical melt pool geometry.

Previous studies have demonstrated that the as-fabricated texture can be altered by changing the scan strategy of a Gaussian laser beam, as described in Section 1. The combination of a flat-top laser beam with a Gaussian beam in the LPBF allows for greater control over the melt-pool geometry and texture formation.

4. Acknowledgments

The authors thank Dr. Takanobu Hiroto, Dr. Miwako Takano, Mr. Masaru Suzuki, Ms. Chiho Togashi, Mr. Koji Nakazato, and Mr. Masahiko Kawasaki of the National Institute for Materials Science for their assistance. This study was supported in part by Amada Foundation (AF-2022215-B3).

5. References

1. T. Ishimoto, H. Hagihara, K. Hisamoto, S.H. Sun, T. Nakano, *Scripta Materialia* 132 (2017) 34–38.
2. L. Thijs, F. Verhaeghe, T. Craeghs, J.V. Humbeek, J.P. Kruth, *Acta Materialia* 58 (2010) 3303–3312.
3. C.M. Cepeda-Jiménez, F. Potenza, E. Magalini, V. Luchin, A. Molinari, M.T. Pérez-Prado, *Materials Characterization* 163 (2020) 110238.
4. A. Carrozza, A. Aversa, P. Fino, M. Lombardi, *Journal of Alloys and Compounds* 870 (2021) 159329.
5. H. Hassanin, Y. Zweiri, L. Finet, K. Essa, C. Qiu, M. Attallah, *Materials* 14 (2021) 2056.
6. D.E. Jodi, T. Kitashima, Y. Koizumi, T. Nakano, M. Watanabe, *Additive Manufacturing Letters* 3 (2022) 100066.
7. S. Pilz, T. Gustmann, F. Günther, M. Zimmermann, U. Kühn, A. Gebert, *Materials and Design* 216 (2022) 110516.
8. P. Ferro, R. Meneghello, G. Savio, F. Berto, *The International Journal of Advanced Manufacturing Technology* 110 (2020) 1911–1921.
9. L. Zeng, T.R. Bieler, *Materials Science and Engineering A* 392 (2005) 403–414.
10. E. Bertrand, P. Castany, T. Gloriant, *Scripta Materialia* 83 (2014) 41–44.